# FLAPW: applications and implementations

## M Weinert[1], G Schneider[2], R Podloucky[3] and J Redinger[4]

[1] Department of Physics, University of Wisconsin-Milwaukee, Milwaukee, WI 53211, USA
[2] Department of Physics, Oregon State University, Corvallis, OR 97331-6507, USA
[3] Department of Physical Chemistry, Sensengasse 8/7, University of Vienna, A-1090 Vienna, Austria
[4] Institut für Allgemeine Physik and Center for Computational Materials Science, Vienna University of Technology, Getreidemarkt 9/134, A-1060 Vienna, Austria

E-mail: weinert@uwm.edu

## Abstract

Modern material design involves a close collaboration between experimental and computational materials scientists. To be useful, the theory must be able to accurately predict the stability and properties of new materials, describe the physics of the experiments, and be applicable to new and complex structures—the all-electron full-potential linearized augmented plane wave (FLAPW) is one such method that provides the requisite level of numerical accuracy, albeit at the cost of complexity. Technical aspects and modifications related to the choice of basis functions (energy parameters, core–valence orthogonality, extended local orbitals) that affect the applicability and accuracy of the method are described, as well as an approach for obtaining $k$-independent matrix elements. The inclusion of external electric fields is illustrated by results for the induced densities at the surfaces of both magnetic and non-magnetic metals, and the relationship to image planes and to nonlinear effects such as second harmonic generation. The magnetic coupling of core hole excitations in Fe, the calculation of intrinsic defect formation energies, the concentration-dependent chemical potentials, entropic contributions, and the relative phase stability of Zr-rich Zr–Al alloys are also discussed.

(Some figures in this article are in colour only in the electronic version)

## 1. Introduction

Modern electronic structure theory based on density functional theory (DFT) [1] has become a standard tool in condensed matter physics, chemistry and materials science for theorists and experimentalists alike. The ability to make detailed predictions of the atomic, electronic and magnetic properties of materials, coupled with experiments, can yield insights that are difficult, if not impossible, to obtain otherwise, and allow one to discriminate among different apparently plausible physical explanations.

The DFT problem is non-trivial. Over the years many different methods and approaches have been proposed and used, all with different strengths and weaknesses. It is somewhat surprising to note that most of the methods and codes in use today trace their roots back decades, albeit with significant improvements and additions. This long timescale reflects the large investment in time (measured in person–years) required to develop code, the pragmatic view of DFT codes as simply tools, the relatively few people directly involved in program development, and the fact that the underlying physical bases for the approaches have not been superseded.

With advances in computational power, it is now possible to tackle problems that were completely out of reach just a few years ago. The fastest—and yet reliable—approaches are based on plane wave basis sets (pseudopotential approaches), where fast Fourier techniques can be heavily exploited such that the Hamiltonian matrix can be built in a fast and efficient way, and allows for efficient iterative diagonalization. Forces and matrix elements are also formally simple and thus straightforward and fast to calculate.

The all-electron augmented methods [2] represent another branch of development. Here space is broken up into spheres

(often called 'muffin-tin' spheres) around the atoms and an interstitial region, and the wavefunctions, density and potential are defined in a piece-wise manner, consisting of some analytic form in the interstitial and numerical solutions inside the spheres. The use of a 'natural' (atomic-like) representation of the wavefunctions around the nuclei allows for an efficient description of the chemical bonding and facilitates the proper treatment of localized properties such as core hole excitations. The augmented plane wave (APW) method [2] uses plane wave representations in the interstitial, but other choices have been (and continue to be) used. In the linearized version (LAPW), two radial functions are used for each angular moment to match the value and derivative across the sphere boundaries so that the variational expressions [3] for the eigenstates do not require surface terms, and since the Hamiltonian is energy-independent, matrix diagonalization can be used. Although Marcus [3] was the first to explicitly write down the LAPW (among other formalisms), Andersen [4] and Koelling and Arbman [5] independently developed the first functional LAPW codes. While the utility of the LAPW method was quickly realized, including for surfaces and film calculations [6], it was also recognized that treating the potential (and density) without shape approximations [7, 8] was essential in order to accurately calculate the properties of low symmetry or ill-packed systems. The difficulty in formulating a full-potential method is related to the solution of Poisson's equation because of the rapid variations in the all-electron charge density near the nuclei and the long-range nature of the Coulomb interaction.

The combination of a general approach to the solution of Poisson's equation [7] for all-electron systems and the LAPW method resulted in the full-potential linearized augmented plane wave (FLAPW) method [9, 10]. This full-potential formulation also provided a natural and numerically stable approach for calculating all-electron total energies [10] that does not suffer from catastrophic numerical cancellation. With total energies and forces [11], the FLAPW method became a method with wide applicability known for its accuracy. But a price has to be paid for this flexibility in terms of computing time and complexity: (i) building the Hamiltonian (and overlap) matrix is costly because of non-spherical matrix elements; (ii) iterative diagonalization is more difficult to implement; (iii) the piece-wise representation and the matching at sphere boundaries introduces a dependence on the chosen spheres, which can be cumbersome when, during structural relaxation, atomic spheres intersect and (iv) the formalism generally is significantly more elaborate and complex to program.

The FLAPW method is actively being developed by at least several different groups [12–15]. In this paper we discuss some technical aspects of our version of FLAPW known as *flair* [12] and some physical applications. Although the original papers provide an overview of the method, many of the improvements incorporated in *flair* related to applicability, user friendliness and extensions have never been published even though they may have been essential in the calculations needed to address physical problems. In section 2 we describe some details and modifications related to the choice of basis

functions that significantly improve the usability of the method compared to standard/original FLAPW. In section 3, we discuss the possibility of rewriting the Hamiltonian matrix elements in a *k*-independent fashion. Then in section 4 we discuss the inclusion of external electric fields and results for image planes of various metal surfaces. Results for the magnetic coupling of core hole excitation in Fe are given in section 5. Finally, the application of DFT calculations to the problem of defects and phase stability in Zr–Al alloys is discussed in section 6.

## 2. Basis functions

The form of the basis functions in the augmented methods is at once both an advantage and a disadvantage. Because the basis functions inside the atomic spheres are numerical solutions using the actual potential, they are effectively optimized for the particular system and by construction fulfill the cusp condition, thus leading to flexible (and accurate) solutions. However, because the basis functions change during the iteration process and have different representations in different regions of space, they significantly complicate the formalism (and programming) and introduce a number of additional parameters such as the sphere radii and energy parameters. In contrast, in plane wave pseudopotential and PAW approaches, the basis functions are simple with nice analytic properties, but the underlying parameters and approximations (such as core radii or cutoffs) are hidden in the generation of the pseudopotentials such that even their existence is not obvious.

### 2.1. Energy parameters

A seemingly trivial issue in the augmented methods is the choice of energy parameters. A misplaced energy parameter may cause problems analogous to the 'ghost' states seen in pseudopotential calculations that arise because a radial basis function (or its energy derivative) is from the wrong branch of the logarithmic derivative. Two related issues are how to choose reasonable energy parameters and then how to specify them. Once choices have been made, it is convenient, as a practical matter, to have the energy parameters chosen and updated automatically.

In the linearized methods, the radial wavefunctions inside the atomic sphere are expressed in terms of numerical solutions of the Hamiltonian, $u_\ell(r; \epsilon_\ell)$, for angular momenta $\ell = 0, 1 \ldots$ at an energy $\epsilon_\ell$ and the corresponding energy derivatives $\dot{u}_\ell(r) \equiv \mathrm{d}u_\ell(r)/\mathrm{d}\epsilon$. By construction, eigenstates whose energies are close to the energy parameter $\epsilon_\ell$ will be given most accurately. Since the states that contribute to the charge density, and hence the total energy, are the occupied states, we choose the energy parameter for a given $\ell$ equal to the center of gravity of the occupied states of that character, which is equivalent to choosing $\epsilon_\ell$ to minimize the rms deviation of the occupied band energies; initially, the energy parameters are set equal to the energies of the corresponding atomic energies. Since during the self-consistency cycle the bands change, sometimes significantly, the energy parameters are updated every iteration. Because the self-consistent density

depends on the energy parameters through the wavefunctions, the energy parameters are part of the specification of the self-consistent density.

   This algorithm provides a well-defined and accurate method for choosing the energy parameters, with the caveat that the program automatically checks for the correct number of nodes to ensure that the $u_\ell(r; \epsilon_\ell)$ is from the correct branch. In a bulk system, however, the zero of the potential is arbitrary and will depend on the convention chosen. For a surface calculation, the situation is somewhat better in that the potential far away from the surface is a natural vacuum zero, but in a film geometry there are possibly two different vacuum zeros. Moreover, the relative energy position of different atoms can change significantly during the self-consistency procedure, especially for compounds. These practical considerations make it problematic to specify the energy parameters on an absolute energy scale.

   Our long-time approach for dealing with this issue is based on the observation that core-level shifts provide a measure of the chemical and physical environment, but the (deep) core levels orbitals themselves do not take part in the bonding or change their shape. (The validity of the frozen core and pseudopotential approximations are based on this behavior.) These core states sample the potential near the nucleus and their energies provide a way to align each atom to a common zero that consistently includes the shifts in the potential. Thus, we choose as the *reference* energy for the energy parameters the value of the potential at a distance $\sim 1/4$ of the atomic sphere radius out from the nucleus, and let the energy parameters themselves 'float'. With this simple device, choosing energy parameters can be done completely automatically throughout the self-consistency cycle because a change in the (local) zero of the potential does not cause a change in the radial basis functions. This same idea of 'floating' energy parameters is also used for the basis functions in the vacuum regions.

## 2.2. Explicit core orthogonalization

The use of floating energy parameters greatly simplifies the practical application of FLAPW (and other augmented methods). However, a significant problem remains related to so-called semi-core states, i.e. states that are often 10–15 eV below the valence bands, but whose radial extent is such that they have significant weight outside the atomic spheres. Typical examples are the shallow p core states at the beginning of the transition-metal rows.

   In principle, any calculation of the eigenstates should include all the (occupied) states, including the core states, as done in a standard LCAO method. Pseudopotential approaches define effective Hamiltonians whose spectra no longer include the core levels and replace the valence wavefunctions by pseudo-functions. In the augmented methods, the Hamiltonian is put into core–valence block diagonal form. Assuming core–valence orthogonality, the core and valence states can be determined separately. This orthogonality is exact for core states completely contained inside the atomic sphere. Let $\hat{h}$ be the radial $\ell$-dependent Hamiltonian and let $u_i$ be the

radial solution at $\epsilon_i$, $\hat{h}u_i = \epsilon_i u_i$, with regular boundary conditions applied at the origin. ($u_i$ is not necessarily an eigenstate of $\hat{h}$ since no condition is placed on the solution at the sphere boundary.) A Wronskian relationship between the two functions $u_i$ evaluated at different energies $\epsilon_i$ is found by integrating over a sphere of radius $S$ to give

$$\langle u_1|\hat{h}|u_2\rangle_S - \langle u_2|\hat{h}|u_1\rangle_S = (\epsilon_2 - \epsilon_1)\langle u_2|u_1\rangle_S$$
$$= \frac{S^2}{2}\left(u_2 u_1' - u_1 u_2'\right)|_{r=S} \quad (1)$$

where $u' \equiv \mathrm{d}u/\mathrm{d}r$. Equation (1) demonstrates that $u_1$ and $u_2$ are orthogonal when $\epsilon_1 \neq \epsilon_2$ *and* the value and derivative of one of the two functions, e.g. $u_2$ (corresponding to a core state), is zero on the sphere boundary. (The second part of equation (1) holds non-relativistically; the corresponding relativistic version is written in terms of $f$ and $g$, the large and small components, respectively, as

$$S^2\left(f_2 cg_1 - f_1 cg_2\right)|_{r=S}, \quad (2)$$

where $cg$ is related to the derivative of $f$ by the radial Dirac equation $cg = \{f' + (\kappa + 1)f/r\}/2(1 + (\epsilon - V)/2mc^2)$.) Similarly, by taking the derivative of equation (1) with respect to $\epsilon_1$:

$$(\epsilon_2 - \epsilon_1)\langle u_2|\dot{u}_1\rangle_S - \langle u_2|u_1\rangle_S = \frac{S^2}{2}\left(u_2\dot{u}_1' - \dot{u}_1 u_2'\right)|_{r=S}, \quad (3)$$

it is easy to see that $\langle \dot{u}_1|u_2\rangle_S = 0$ under the same conditions.

   Because the decay of the core states is exponential, the orthogonality between the core levels and the radial basis functions $u_\ell$, $\dot{u}_\ell$ over the sphere is only approximate (becoming exact as $s \to \infty$). Although this approximation is quite accurate for deep core levels, it becomes problematic as the core levels become shallower and more extended, or if the spheres become smaller so that the off-diagonal core–valence terms become larger. The relative amount of the core density outside the sphere provides a measure of this non-orthogonality. Once the semi-core charge outside the atomic sphere starts to become significant, problems arise with ghost states and other numerical instabilities; these most often first show up as increasing contributions of $\dot{u}_\ell$ to the wavefunctions, resulting from increasing linear dependence (overlap) of $\dot{u}_\ell$ and the semi-core state.

   To deal with these issues a number of different approaches have been used over the years. The simplest is to raise the energy parameter, thereby increasing the energy separation, and decreasing the overlap of the core and valence states. Unfortunately, this approach seldom works and, when it appears to, it often requires unreasonable increases in the energy parameters such that the function actually is from the next branch corresponding to a higher principal quantum number. Conversely, the energy parameter can be lowered near the energy of the semi-core level so that the semi-core states are treated as valence states. Although this approach solves the ghost state problem, it also drastically reduces the variational freedom describing valence states of that $\ell$ character. Whether that lost accuracy is important depends on the system.

   Another common approach is the use of so-called 'local orbitals' [16]. The semi-core states are included in the valence

band by introducing another radial function, $u_{\text{lo}}$, with its energy parameter set to the semi-core energy. The local orbitals (LO) are defined to have zero value and derivative on the sphere boundary—which requires that the LO has significant $u_\ell$ and $\dot{u}_\ell$ contributions—and are then coupled to 'fictitious' plane waves. In this way both the valence and semi-core states are obtained in a single diagonalization, ensuring orthogonality. Compared to the approach of simply moving the energy parameter down to the semi-core state, the valence states are described by $u_\ell$ and $\dot{u}_\ell$ in the valence region. However, since the extra LO basis functions and their derivatives are required to vanish at the sphere boundary, they do a poor job by themselves of describing the semi-core states: if they did describe the semi-cores well, the LOs would not be needed since, by equation (1), the semi-core and valence states would already be orthogonal. As obtained from the diagonalization, the semi-core eigenstates must be a mixture of the LOs plus a large number of 'normal' LAPWs in order to recover the correct $u_{\text{lo}}$ radial behavior and to describe the decaying tails in the interstitial. Moreover, variational calculations by their nature describe the lowest (i.e. semi-core states) most accurately so errors in those states will affect the accuracy of the valence states through the orthogonalization. Thus, to describe both the semi-core and valence states accurately, this approach requires larger basis sets than the standard LAPW method. Even with these complications, the use of the LO in this manner provides one reasonably straightforward way to deal with the semi-core issues.

When the semi-core states do not have significant overlap and bonding with atoms on other sites, a separation between valence and (semi-)core states is physically reasonable. Here, we present a modification of the (F)LAPW method that, in this case, (i) deals with the valence–semi-core orthogonalization explicitly, (ii) is easy to implement and (iii) maintains variational freedom in the valence regime. For situations where the semi-core states have significant overlap with other sites, their spatial extent (and tails) and energy dependence should be treated explicitly (cf. section 2.3).

To remove the core state(s) $|c\rangle$ from the spectrum of a Hamiltonian $\hat{H}$, we can define a modified Hermitian Hamiltonian

$$\tilde{H} = \{1 - |c\rangle\langle c|\}\,\hat{H}\,\{1 - |c\rangle\langle c|\} \tag{4}$$

such that $\tilde{H}|c\rangle = 0$ and $\tilde{H}|v\rangle = \hat{H}|v\rangle$ ($|v\rangle$ corresponds to a valence eigenstate), i.e. $\tilde{H}$ has the same valence eigenstates as $\hat{H}$, but does not include the core states. Rather than change the Hamiltonian (as done in pseudopotential approaches), one can apply the projection operator $\{1 - |c\rangle\langle c|\}$ to the basis functions. ($|c\rangle$ is, in the case of semi-cores, non-zero outside the sphere and thus $\langle c|u_\ell\rangle_S \neq 0$ over the sphere.) Applying this operator to the FLAPW radial basis function $u_\ell$ directly is not appropriate since, for eigenstates with energy equal to $\epsilon_\ell$, this function has the correct radial behavior and nothing in the (projected) basis would be able to recover the missing part.

Since $u_\ell$ is needed in the basis and problems often manifest themselves in the energy derivative contributions, we replace the energy derivative by a modified function:

$$|\dot{w}_\ell\rangle = |\dot{u}_\ell\rangle + \alpha|c\rangle + \beta|u_\ell\rangle. \tag{5}$$

Requiring this function to be orthogonal over the sphere to both $u_\ell$ and the uppermost core state $c$ of this $\ell$:

$$\langle \dot{w}_\ell|u_\ell\rangle_S = 0 \tag{6}$$

$$\langle \dot{w}_\ell|c\rangle_S = 0, \tag{7}$$

and using $\langle \dot{u}_\ell|u_\ell\rangle_S = 0$, $\langle u_\ell|u_\ell\rangle_S = 1$, yields (dropping the $S$ subscript on the inner products)

$$|\dot{w}_\ell\rangle = |\dot{u}_\ell\rangle - \frac{\langle c|\dot{u}_\ell\rangle}{\langle c|c\rangle - \langle u_\ell|c\rangle\langle c|u_\ell\rangle}\Big[|c\rangle - |u_\ell\rangle\langle u_\ell|c\rangle\Big]. \tag{8}$$

For core states completely contained in the spheres, $\dot{w}_\ell$ is identical to the normal energy derivative $\dot{u}_\ell$. Since $u_\ell$ and $\dot{w}_\ell$ are independent functions, the continuity of the LAPW basis functions is maintained (provided the Wronskian does not vanish), so no additional surface terms are needed.

The use of $\dot{w}_\ell$ instead of $\dot{u}_\ell$ requires relatively few changes since it is simply a different radial function. The Wronskian between $\dot{w}_\ell$ and $u_\ell$, which comes into the matching conditions at the sphere boundary:

$$u_\ell \dot{w}_\ell' - u_\ell' \dot{w}_\ell = \left(u_\ell \dot{u}_\ell' - u_\ell' \dot{u}_\ell\right) - \frac{\langle c|\dot{u}_\ell\rangle}{\langle c|c\rangle - \langle u_\ell|c\rangle\langle c|u_\ell\rangle}$$
$$\times \Big[u_\ell c' - u_\ell' c\Big] \tag{9}$$

is no longer a constant as for $u_\ell$ and $\dot{u}_\ell$ (cf. equation (3)). However, as a practical matter for reasonably sized spheres (where less than about 30% of the semi-core density is outside the sphere) the correction to the Wronskian between $u_\ell$ and $\dot{u}_\ell$ is small and the Wronskian remains non-zero.

To obtain the modified contributions to the Hamiltonian, note that $\dot{w}_\ell$ satisfies

$$\hat{h}|\dot{w}_\ell\rangle = \epsilon_\ell|\dot{w}_\ell\rangle + |u_\ell\rangle + (\epsilon_\ell - \epsilon_c)\frac{\langle c|\dot{u}_\ell\rangle}{\langle c|c\rangle - \langle u_\ell|c\rangle\langle c|u_\ell\rangle}|c\rangle, \tag{10}$$

which, except for the last term involving $|c\rangle$, is the same as the equation for $\dot{u}_\ell$. The contributions to the Hamiltonian in the spheres are

$$\langle u_\ell|\hat{h}|u_\ell\rangle = \epsilon_\ell \tag{11a}$$

$$\langle \dot{w}_\ell|\hat{h}|u_\ell\rangle = 0 \tag{11b}$$

$$\langle u_\ell|\hat{h}|\dot{w}_\ell\rangle = 1 + (\epsilon_\ell - \epsilon_c)\frac{\langle c|\dot{u}_\ell\rangle\langle u_\ell|c\rangle}{\langle c|c\rangle - \langle u_\ell|c\rangle\langle c|u_\ell\rangle} \tag{11c}$$

$$\langle \dot{w}_\ell|\hat{h}|\dot{w}_\ell\rangle = \epsilon_\ell\langle \dot{w}_\ell|\dot{w}_\ell\rangle. \tag{11d}$$

Compared to the standard LAPW Hamiltonian contributions, the only change (other than the replacement of $\dot{u}_\ell$ by $\dot{w}_\ell$) is the inclusion of the last term in equation (11c). Non-spherical contributions to the Hamiltonian, forces, potentials, total energies, etc, are all calculated in the standard ways.

This modified form of the energy derivative, nicknamed 'explicit orthogonalization' (XO), has been used routinely over the last few years. Whereas previously even simple systems (e.g. Ge, KCl) could present problems, this approach is quite robust. From a variational point of view for functions inside the sphere, explicitly projecting out the semi-core states from the valence basis (the energy derivative) provides the same variational freedom as including another radial function

with energy parameter $\epsilon_c$ since both approaches span the same space, $u_\ell$, $\dot{u}_\ell$, and $c_\ell$. By explicitly orthogonalizing to the core state, the Hamiltonian is effectively block (core +valence) diagonalized. On the other hand, $u_\ell$, $\dot{u}_\ell$, and $u_{lo}$ form a set of non-orthogonal axes in function space, requiring a diagonalization of the full space. As a practical matter, the various functions are not free to vary completely independently because of the continuity conditions across the sphere boundary imposed and the limited basis size. In such cases, it is generally preferable to start with basis functions that are as close to being diagonal as possible; that these types of continuity conditions play a role in convergence is known both from comparison to the APW method and to linearized methods such as LASTO [17] that have smaller basis sets and hence are more limited in the combinations of $u$ and $\dot{u}$ that can be constructed. Based on experience, the XO approach provides good variational freedom and has the advantage of smoothly going over to the standard FLAPW.

### 2.3. Extended local orbitals

The explicit orthogonalization described above is appropriate when the semi-core states do not have significant overlap with other atoms. If there is significant overlap, the description of the tails of functions centered on one site at another site is difficult. Use of the XO approach discussed above neglects the interactions of this state on different sites, and thus ignores, for example, core–core repulsion effects. Including the semi-core using the 'local-orbital' [16] approach by including the LO explicitly in the valence would seem to improve upon this situation. Unfortunately, the situation is more complicated. Consider a semi-core state with energy $\epsilon_c$. If at a neighboring site there are no semi-core states, then the tails inside that sphere must be described by the *valence* $u_\ell$, $\dot{u}_\ell$, whose $\epsilon_\ell$ is off by 10–20 eV, and hence will often be in the wrong branch. This could be remedied by including LOs on the neighboring site with the corresponding $\epsilon_c$. However, these (secondary) LOs would not correspond to a single $\ell$, since the expansion about another site involves higher angular momenta [18]. Thus, for consistency, every (primary) LO should have a corresponding set of LOs on every other site. The standard approximation of ignoring these issues generally leads to reasonable physical results, but it is difficult *a priori* to determine the magnitude of the resulting error. This problem is not unique to the augmented methods; approaches based on, for example, norm-conserving pseudopotentials or finite number of projectors inherently have similar issues although these complications are conveniently ignored in the construction of the pseudopotentials.

To deal with situations where the spatial extent of the semi-core or localized valence states (e.g. 4f states) is important, we propose supplementing the basis with Bloch sums $\chi_k^\alpha(\mathbf{r})$ of atomic-like functions $\phi^\alpha$:

$$\chi_k^\alpha(\mathbf{r}) = \frac{1}{\sqrt{N}} \sum_{\mathbf{t}} e^{i\mathbf{k}\cdot\mathbf{t}} \phi^\alpha(\mathbf{r} - \mathbf{t} - \mathbf{r}_\alpha) \qquad (12)$$

where $\mathbf{t}$ is a lattice translation vector, $\alpha$ denotes both an atom and atomic state, $\mathbf{r}_\alpha$ is the position of the atom in the unit cell and $N$ is the number of unit cells with the crystal.

The criteria for the atomic-like—'extended local orbitals' (elo)—functions $\phi^\alpha(\mathbf{r}) = \phi^\alpha(r)Y_{\ell m}(\hat{r})$ are that the radial function $\phi^\alpha(r)$ for $r > S$ should closely resemble the tails of the semi-core states and, secondarily, have analytic properties that simplify expansions about other sites. Possible choices include Slater-type orbits and, our current favorite, modified spherical Bessel functions of the third kind, $k_\ell(\kappa r)$ [19], where $k_0(z) = (\frac{1}{2}\pi/z)e^{-z}$, $k_1(z) = (\frac{1}{2}\pi/z)e^{-z}(1 + z^{-1})$, etc. These functions are solutions for negative energies relative to a muffin-tin potential and can be expanded about another site using the Gegenbauer addition theorem [19, 20] to obtain

$$k_\ell(\kappa|\mathbf{r} + \mathbf{R}|)Y_{\ell m} = \sum_{L'L''} 4\pi(L|L'L'')(-1)^{\ell''}k_{\ell'}(\kappa R)i_{\ell''}(\kappa r)$$
$$\times Y_{L'}(\mathbf{R})Y_{L''}(\mathbf{r}) \qquad (13)$$

where $(L|L'L'')$ is a Gaunt coefficient, $i_\ell(z)$ is a modified spherical Bessel function of the second kind and $R > r$. At the sphere boundary, the requirement that this function matches the numerical (semi-core) radial function $c_l(r)$, evaluated at $\epsilon_c$ determines $\kappa$. Note that the analytic form of $\phi^\alpha$ is only needed outside the sphere. The matching of the standard LAPWs in the basis set are done using the $u_\ell$ and $\dot{w}_\ell$ functions discussed above. If one wanted to include an additional radial function in the spheres, for example the energy derivative of $c_\ell$ to better describe the energy variation of the semi-core band, an additional set of $\phi$s such as the energy derivatives of the $k_\ell$ should be included.

In order to avoid the problems of requiring additional radial functions in each secondary sphere, the tails of $\phi$ are used explicitly, i.e. they are not expanded in terms of the $u_\ell$, etc, in those spheres. This treatment of the tails is effectively an LCAO-type approximation. The extended local orbit contributions to the Hamiltonian and overlap matrices are broken up into interstitial and sphere terms.

The tails are treated in two related ways. In the first, the atomic-like functions $\phi(\mathbf{r})$ are Fourier-transformed, using a much larger **G** cutoff than is used to define the basis set, and then combined to build up the Bloch functions. (To improve the convergence of the Fourier transform of $\phi$, $\phi(r)$ is replaced by a polynomial inside the sphere.) In this case, the Fourier expansion, rather than the Bloch expansion equation (12), defines the additional functions everywhere except in the sphere $\alpha$, where the function is defined by the numerical solution. This approach is similar to how the linearized augmented Slater-type orbital (LASTO) method [17] was implemented and is reasonably straightforward to implement. The most difficult terms are the tail-$u_\ell$ terms since the Fourier representation of the tails must be expanded on the radial mesh in order to do the necessary integrals.

The second approach is to make a tight-binding approximation so that for any sphere only the tails from a few neighboring sites are included. To calculate the interstitial terms, the potential and/or APWs are expanded in a spherical harmonic representation. In the spheres, the tails are re-expanded using standard expansion theorems [19] such as equation (13). The type of operations needed are similar to the LCAO methods.

In both approaches, the sphere terms are straightforward once a numerical expansion of the tail terms is made in the

spheres, $\sum_{\lambda\mu} \phi_{\lambda\mu}^{\alpha\beta}(r') Y_{\lambda\mu}(\mathbf{r}')$, where $\mathbf{r}' = \mathbf{r} - \mathbf{r}_\beta$. For the LAPW-elo off-diagonal terms in the sphere $\alpha$, $\langle\chi^\alpha|\hat{H}|\mathbf{G}\rangle_\alpha$ will consist of terms as discussed in section 2.2, e.g. $\langle u_\ell|\hat{h}|c_\ell\rangle$. For spheres centered on a different site $\beta$, $\langle\chi^\alpha|\hat{H}|\mathbf{G}\rangle_\beta$ will have terms such as $\langle\phi_{\lambda\mu}^{\alpha\beta}|\hat{h}|\dot{w}_\ell\rangle$. For contributions that consist of tails from two sites (or different orbitals), these can be done either numerically or analytically, depending on the choice of tail. The interstitial contributions require a Fourier transform of the tails. The calculation of densities follows directly from the representation of the extended local orbitals.

The use of the extended orbitals should improve the convergence with respect to basis size for cases when semi-cores, or low-lying/compact valence states such as the oxygen 2s or 4f states, are important. Including the extended local orbitals is not free, but by using the tight-binding-like representation the scaling is linear, albeit with a reasonably large prefactor. Modifications are required for the force calculations because of the atom-centered and extended nature of the additional basis functions.

## 3. k separation of the Hamiltonian matrix

As discussed above, augmenting the plane wave basis of the (L)APW with atomic-like functions inside an atomic sphere of radius $R_\alpha$ centered at $\mathbf{r}_\alpha$ requires matching conditions on the sphere boundary after the plane wave $\exp(\mathrm{i}(\mathbf{k}+\mathbf{G})\cdot\mathbf{r})$ ($\mathbf{k}$ in the first Brillouin zone and $\mathbf{G}$ a reciprocal lattice vector) is expanded into spherical harmonics and spherical Bessel functions around the atomic position $\mathbf{r}_\alpha$. These augmented basis functions naturally depend also on $\mathbf{k}$. In the LAPW [4, 5], where the values and first derivatives are matched, the basis functions inside the spheres are written as

$$\Phi_L^\alpha(\mathbf{k}+\mathbf{G}, \mathbf{r}) = \{a_L(\mathbf{k}-\mathbf{G})u_\ell(|\mathbf{r}-\mathbf{r}_\alpha|)$$
$$+ b_L(\mathbf{k}-\mathbf{G})\dot{u}_\ell(|\mathbf{r}-\mathbf{r}_\alpha|)\}Y_L(\mathbf{r}-\mathbf{r}_\alpha) \quad (14)$$

for a given set $L = (\ell, m)$ of angular momentum quantum numbers. The matching coefficients $a_L$, $b_L$ contain the $\mathbf{k}$-dependent spherical harmonics and Bessel functions. In the original APW ansatz the explicit $\mathbf{k}$ dependence consists of terms diagonal in $L$ because of the restriction to spherically symmetric ('muffin-tin') potentials inside the spheres, and therefore this dependence was not a major concern. However, in FLAPW calculations a substantial price has to be paid because three $L$ summations are required in the Hamiltonian (potential) matrix elements inside sphere $\alpha$:

$$\langle\mathbf{k}+\mathbf{G_1}|V^\alpha|\mathbf{k}+\mathbf{G_2}\rangle$$
$$= \sum_{L'}\sum_{L}\sum_{L''} \langle\Phi_{L'}^\alpha(\mathbf{k}+\mathbf{G_1})|V_L Y_L|\Phi_{L''}^\alpha(\mathbf{k}+\mathbf{G_2})\rangle. \quad (15)$$

The expansion of the potential $V = \sum_L V_L Y_L$ should be made to at least twice the $\ell_{max}$ for the wavefunction. This costly evaluation has to be done for each $k$ point separately due to the $\mathbf{k}$ dependence of the matching coefficients.

Switching to simple plane waves, $\exp(\mathrm{i}(\mathbf{k}+\mathbf{G})\cdot\mathbf{r})$, as basis functions for the whole of space, the potential matrix element is independent of $\mathbf{k}$ simply because the Bloch factor $\exp(\mathrm{i}\mathbf{k}\cdot\mathbf{r})$ cancels out: only the kinetic energy terms are $\mathbf{k}$-dependent and the Hamiltonian matrix elements are

$$\langle\mathbf{k}+\mathbf{G_1}|\hat{H}|\mathbf{k}+\mathbf{G_2}\rangle = (\mathbf{k}+\mathbf{G_2})^2\delta_{\mathbf{G_1},\mathbf{G_2}} + \langle\mathbf{G_1}|V|\mathbf{G_2}\rangle. \quad (16)$$

The potential $V$ has the full symmetry of the lattice, and therefore may be Fourier-expanded as $V(\mathbf{r}) = \sum_\mathbf{G} V_\mathbf{G}\exp(\mathrm{i}\mathbf{G}\cdot\mathbf{r})$ by summing over the reciprocal lattice vectors. This convenient representation makes plane-wave-based approaches very attractive for fast and efficient calculations. Of course, the price to pay here is that a full potential cannot be realistically described, and therefore suitable pseudopotentials have to be constructed, a task that is not straightforward. However, schemes like the projector augmented wave (PAW) concept [21, 22] seem to be reliable in modeling the valence electronic structure of systems even with very localized states.

The aim of the present discussion is to pursue the idea of $\mathbf{k}$-independent potential matrix elements for the FLAPW method. We reformulate the ansatz for the basis functions inside the spheres by explicitly pulling out the Bloch factor and considering

$$\Phi_L^\alpha(\mathbf{k}+\mathbf{G}, \mathbf{r}) = \mathrm{e}^{\mathrm{i}\mathbf{k}\cdot\mathbf{r}}\Phi_L^\alpha(\mathbf{G}, \mathbf{r}). \quad (17)$$

Now only the $\mathbf{k}$-independent part of the basis function $\Phi_L^\alpha(\mathbf{G_1}, \mathbf{r})$ is matched to the $\mathbf{k}$-independent part of the plane wave, $\exp(\mathrm{i}\mathbf{G}\cdot\mathbf{r})$. It is then obvious that one gets an expansion similar to equation (14) for $\Phi_L^\alpha(\mathbf{G}, \mathbf{r})$, but the matching coefficients $a_L$, $b_L$ are now independent of $\mathbf{k}$ and, consequently, the potential matrix elements are also $\mathbf{k}$-dependent, as in equation (16) for simple plane wave basis sets. Making use of the basis function of equation (17) leads to a Hamiltonian matrix element inside sphere $\alpha$ (in atomic units):

$$\langle\Phi^\alpha(\mathbf{k}+\mathbf{G_1})|\hat{H}|\Phi^\alpha(\mathbf{k}+\mathbf{G_2})\rangle$$
$$= \frac{k^2}{2}\langle\Phi^\alpha(\mathbf{G_1})|\Phi^\alpha(\mathbf{G_2})\rangle \quad (18a)$$
$$- \mathrm{i}\mathbf{k}\cdot\langle\Phi^\alpha(\mathbf{G_1})|\nabla\Phi^\alpha(\mathbf{G_2})\rangle \quad (18b)$$
$$+ \langle\Phi^\alpha(\mathbf{G_1})|\hat{H}^{\mathrm{FLAPW}}|\Phi^\alpha(\mathbf{G_2})\rangle. \quad (18c)$$

(For simplicity, the summations over all the different $L$'s are not written explicitly.) The last term, equation (18c), is just the matrix element within the standard FLAPW formulation, including the non-spherical potential matrix elements. The $\mathbf{k}$ dependence of $\langle\hat{H}^{\mathrm{FLAPW}}\rangle$ has disappeared, as desired, but at a price: two additional terms appear, because one has to perform derivatives of the product $\Phi$ times the Bloch factor $\exp(\mathrm{i}\mathbf{k}\cdot\mathbf{r})$. The first kinetic energy term, equation (18a), is just the overlap $S$ matrix element inside the spheres:

$$S^\alpha(\mathbf{k}+\mathbf{G_1}, \mathbf{k}+\mathbf{G_2}) = S^\alpha(\mathbf{G_1}, \mathbf{G_2})$$
$$= \langle\Phi^\alpha(\mathbf{G_1})|\Phi^\alpha(\mathbf{G_2})\rangle \quad (19)$$

multiplied by the constant factor $k^2/2$. Note that $S$ is now also independent of $\mathbf{k}$, which is not the case in the original FLAPW ansatz. The final remaining term, equation (18b), contains the matrix element of the gradient $\nabla\Phi$, for which the scalar

product with the constant vector **k** needs to be done. The key question is how costly the evaluation of this second kinetic energy contribution might be. Transforming $\nabla$ into polar coordinates results in two differential operators. The operator $\nabla_r$ acts on the radial wavefunctions, and its components are multiplied by some linear combination of the spherical harmonics $Y_{11}$, $Y_{10}$, $Y_{1-1}$. Calculating the matrix elements for $\nabla_r$ involves an integral over three spherical harmonics, such as $\int Y_{L'}^* Y_{1m} Y_{L''} d\Omega$, resulting in $\sim l_{max}^2$ evaluations of the matrix element. The second operator $\nabla_\Omega$ acts on angular coordinates, i.e. on the spherical harmonics $Y_{\ell m}$, and produces another set of harmonics $Y_{\ell \pm 1, m \pm 1}$. The number of evaluations of the matrix element is therefore only of order $\sim \ell_{max}$, because of the orthonormal properties of the spherical harmonics. Finally, one notices that—again—the matrix element itself is independent of **k**.

Summarizing, separating out the vector **k** from the FLAPW basis functions in the spheres results in the major advantage that all costly matrix elements now become independent of **k**. They need to be calculated only once, for example for the first **k** point, and then used for building the Hamiltonian for the other remaining **k** vectors. Certainly, for medium to larger basis sizes, even writing to and reading from disk is much faster than calculating the cumbersome non-spherical potential matrix elements. Achieving a significant speed-up of matrix building might aid in applying the very efficient iterative diagonalization techniques of plane wave codes to the FLAPW method. Using the separation ansatz of (17) has further consequences, e.g. for calculating the charge density for which one might apply the same storage technique as described above. Of course, forces and related concept results that depend on the explicit form of the wavefunctions have to be re-derived. The price to be paid seems to be rather moderate, but so far no real tests have been performed; actual tests will be done in the near future.

Finally, we note that the presented mathematical concept is not new, and was suggested for the so-called **k** · **p** method (see, e.g., [23]) that was originally designed as an interpolation scheme for deriving eigenvalues on a finer grid of **k** vectors than originally used for the actual full solution of Schrödinger's equation. However, we emphasize that, although formally similar to the **k** · **p** method, the **k** separation reformulates the Hamiltonian, for which the eigenvalue problem is solved in its full glory.

# 4. External electric fields

External electric fields are integral to a number of experimental techniques, including scanning tunneling microscopy and field desorption microscopy, and are used to alter the electronic properties of (nano)structures. Classical electrostatics describe the effect of electric fields and introduces concepts such as image charges. Calculations allow us to make the connections between these classical concepts and their underlying quantum mechanical basis. For example, the static image plane can be obtained from the center of gravity of the screening charge induced by a weak applied field [24–27], and second harmonic

generation is related to the nonlinear response of the electron gas to stronger applied electric fields [28, 29].

Including external electric fields in a standard electronic structure calculation is problematic since the resulting potential is not periodic. Within the film geometry of the FLAPW method, however, the external electric fields can be included straightforwardly. Although this approach as been used for a long time [30–33], the implementation has not been described previously [30, 34].

## 4.1. Inclusion of a static external field

Including external fields within density functional theory is in principle straightforward: an additional term of the form

$$\int d\mathbf{r}\, V_{ext}(\mathbf{r}) n(\mathbf{r}) \tag{20}$$

is added to the energy functional, where $V_{ext}$ is the potential associated with the field and $n(\mathbf{r})$ is the electron (number) density. For the usual case of the external field due to the atomic nuclei, $V_{ext} = -Z/r$.

An external field, and its corresponding potential, can be related to a charge distribution $\rho_{ext}(\mathbf{r})$ via Poisson's equation

$$\nabla^2 V_{ext}(\mathbf{r}) = -4\pi \rho_{ext}(\mathbf{r}). \tag{21}$$

For a system with two-dimensional periodicity, we can write the density and potential in a two-dimensional Fourier expansion, e.g.

$$V(\mathbf{r}) = \sum_{\mathbf{G}_\parallel} V(\mathbf{G}_\parallel, z) e^{i\mathbf{G}_\parallel \cdot \mathbf{r}_\parallel}. \tag{22}$$

In this representation, the Poisson equation separates into

$$\left[ \frac{\partial^2}{\partial z^2} - G_\parallel^2 \right] V(\mathbf{G}_\parallel, z) = -4\pi \rho(\mathbf{G}_\parallel, z). \tag{23}$$

For the uniform field, we need to consider the $\mathbf{G}_\parallel = 0$ term only. To specify the solution of this second-order equation requires two boundary conditions. Integrating this equation, using mixed boundary conditions at $z = z_0$ ($z < z_0$), gives the potential in terms of the density as (we drop the $\mathbf{G}_\parallel = 0$ label for simplicity)

$$V(z) = V(z_0) - (z_0 - z)\left( \frac{\partial}{\partial z} V(z)\Big|_{z=z_0} \right)$$
$$- 4\pi \int_z^{z_0} dz'\, \rho(z')(z' - z). \tag{24}$$

In the normal zero-field case, $z_0 \to \infty$. For the $\mathbf{G}_\parallel \neq 0$ terms, equation (23) is solved using the Green's function $G(z, z') = 2\pi \exp(-G_\parallel |z - z'|)/G_\parallel$, resulting in contributions to the potential of the form $\exp(i\mathbf{G}_\parallel \cdot \mathbf{r}_\parallel \pm G_\parallel z)$.

Because of the linearity of Poisson's equation, we are free to pick these boundary conditions in any convenient manner. One choice to include the electric field sets $(\partial/\partial z) V(z)|_{z_0} = -E$; in this case, no $\rho_{ext}$ is required to describe the field. Likewise, one can apply two-point boundary conditions, giving the potential at opposite sides of a film. These choices are

useful when, for instance, specifying the potential drop across a film.

Another choice, with a different physical interpretation, is to require

$$V(\infty) = 0, \tag{25}$$

$$\frac{\partial}{\partial z} V(\infty) = 0, \tag{26}$$

consistent with the boundary conditions for the zero-field case, and requires an external charge distribution $\rho_{ext}$ to describe the field. To represent the uniform electric field, elementary electrostatics gives that a planar sheet of charge with surface density $\sigma = q/A$ ($q$ is the total charge and $A$ is the area) will generate a normal field $\mathbf{E} = 4\pi\sigma\hat{\mathbf{n}}$. To determine the magnitude of this surface charge, first note that because of the long-range nature of the Coulomb interaction, the electrostatic energy is well-defined only for systems with total—electrons, nuclei, plus charge sheet—charge neutrality; this requirement is also imposed in the standard zero-field case. With this charge neutrality condition, the potential at $z = -\infty$ is, from equation (24),

$$
\begin{aligned}
V(-\infty) &= -4\pi \int_{-\infty}^{+\infty} \mathrm{d}z z \rho(z) \\
&= -4\pi \int_{-\infty}^{+\infty} \mathrm{d}z z (\rho_{ext} + \rho_i),
\end{aligned}
$$

and $\mathrm{d}V(-\infty)/\mathrm{d}z = 0$, where $\rho_i$ is the induced density. Thus, we have the physically reasonable result that the change in potential across the film is related to the dipole moment of the external and induced densities.

Thus, to include the external field, we can place a sheet of charge 'far enough' outside the surface so that the electrons have negligible overlap with the sheet; this distance is typically 6–10 Å from the last row of atoms. These sheets have charges of the order of $\pm 0.005$–$0.05e$ per unit cell, corresponding to fields $\sim 0.1$–1 V Å$^{-1}$, and then the total number of electrons in the film is adjusted accordingly to satisfy the charge neutrality condition. The *sign* of the electric field is chosen such that, for a positive (negative) electric field, there are fewer (more) total electrons in the system. Because the sheet of charge can be considered as another set of charges completely analogous to the atomic nuclei, albeit in the vacuum region, the same procedures for solving Poisson's equation [7, 9] as used for the zero-field case can be used. In particular, the explicit contribution from the sheet of charge need only be calculated in the vacuum region; the contributions of the electric field in the interstitial and sphere regions are included correctly through the modified boundary conditions at the vacuum–interstitial interface.

Although the external field is uniform, the resulting induced changes in the density and total potential have $\mathbf{G}_\parallel \neq 0$ contributions. Our implementation of the electric field correctly determines these contributions, as well as properly including the boundary conditions. Since an external field necessarily destroys the translational symmetry of the problem perpendicular to the surface, film and/or semi-infinite [26] treatments provide a natural (and rigorous) treatment of electric field effects. For completeness, we point out that electric fields

can also be included in periodic bulk supercell models [36–38] by placing an external electric dipole layer in the vacuum region of the supercell, with the dipole potential updated each iteration to ensure the proper boundary conditions.

An important implementation issue to consider in any film geometry is the representation of the Coulomb potential to use. In particular, to get the spherical (lattice) harmonic representation on the atomic spheres, one should directly expand the exponential terms $\sim \exp(\mathrm{i}\mathbf{G}_\parallel \cdot \mathbf{r}_\parallel \pm G_\parallel z)$ resulting from (23) using the analytic expansion of the 'complex' plane waves [7], rather than first converting them into the normal 3D Fourier representation used in the interstitial region.

### 4.2. Induced densities and image planes

To illustrate the application of external fields, we consider how external fields are screened at the surface of metals. The electron density $n$ in a static external field $E$ can be expanded as

$$n(z, E) = n_0(z) + E n_1(z) + E^2 n_2(z) + \cdots. \tag{27}$$

As shown by Lang and Kohn [25], the image plane is related to the centroid of the induced density, $\delta n(z) \equiv (n(z, E) - n_0)/E$:

$$z_{image}^0 = \frac{\int \mathrm{d}z z n_1(z)}{\int \mathrm{d}z n_1(z)} \tag{28a}$$

$$z_{image}(E) = z_{image}^0 + E \int \mathrm{d}z z n_2(z) + \cdots. \tag{28b}$$

For time-dependent fields, $E(t) = E_0 \sin\omega t$, where the frequency is much less than the plasmon frequency so that one is in the adiabatic response regime, the time- and field-dependent density can be written [28] in terms of the static response:

$$n(z, t) = n_0(z) + E(t)n_1(z) + E^2(t)n_2(z) + \cdots \tag{29a}$$

$$= [n_0(z) + \tfrac{1}{2}E_0^2 n_2(z) + \cdots] + [E_0 n_1(z) + \cdots]\sin\omega t$$
$$+ [-\tfrac{1}{2}E_0^2 n_2(z) + \cdots]\cos 2\omega t + \cdots \tag{29b}$$

$$\equiv n_{dc}(z) + n_\omega(z)\sin\omega t + n_{2\omega}(z)\cos 2\omega t + \cdots. \tag{29c}$$

In particular, the second harmonic density $n_{2\omega}$ is related [28] to the second-order $n_2$ static-induced density, and then the longitudinal second harmonic current is proportional to the second-order polarization:

$$P_2(z) = \int_z^\infty \mathrm{d}z' n_2(z'). \tag{30}$$

The overall strength of second harmonic generation (SHG) is proportional to the integral of $P_2(z)$ or, equivalently, the centroid of the static second-order contribution $n_2(z)$. To extract $n_1(z)$, $n_2(z)$, etc, we first calculate the induced density for a series of positive and negative static external fields.

As an illustration, the calculated induced densities for the (001) and (110) faces of bcc Na, and for jellium at $r_s = 4$ appropriate to Na, are given in figure 1(a). The induced density is strongly peaked in the surface region, and then oscillates and decays with a characteristic period into the bulk that is *not* tied to the atomic positions. The calculated positions of the image plane to the jellium edge (atomic plane) are 1.82
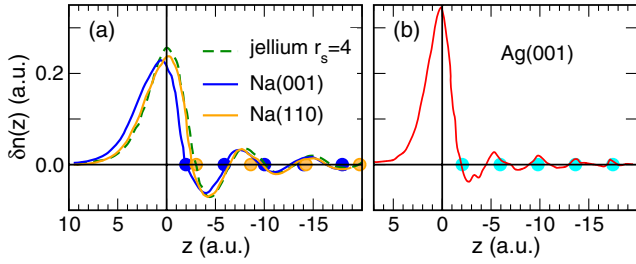
**Figure 1.** Induced densities for (a) the (001) and (110) surfaces of Na and for the corresponding jellium of $r_s = 4$, and (b) Ag(001). The jellium edge, defined as half the interlayer separation from the surface atomic positions, is at $z = 0$. Positions of the atoms are denoted by the filled circles. The densities are normalized to unity.

(3.96), 1.38 (3.80) and 1.25 $a_B$ for the (001), (110), and jellium systems, respectively. The jellium and (close-packed) (110) results are quite similar, and the differences compared to the (001) surface are localized in the surface region. The difference in the position of the image plane between the two surfaces is a result of the atomic nature (size) of the actual system, and consistent with the trends obtained from a simple model related to the image states [35]. All three systems are calculated to have very similar SHG strengths.

In figure 1(b) the induced density for Ag(001) is shown. Compared to Na, the width of $\delta n$ is smaller, the image plane is in closer, the SHG strength is lower than for Na, and the oscillations into the bulk are associated with the atomic positions. In contrast, jellium calculations for $r_s = 3$ (corresponding to Ag) predict an image plane further out ($\sim$0.1 au) compared to $r_s = 4$, as well as stronger SHG for Ag than for Na. These results point to the Ag surface being 'stiffer' than jellium and are a consequence of the d-electron screening of Ag that is not found in Na or jellium.

Electric fields can couple differently to different spin channels in magnetic systems, resulting in electric-field-induced magnetic effects [32]. In figure 2(a) the induced charge and spin densities are shown for Fe(001). The first-order-induced charge $n_1$ is strongly localized to the surface

region, with its centroid (the image plane) outside the surface atomic layer, again demonstrating the importance of both sp and d electrons to the screening. The corresponding induced spin density, on the other hand, is shifted inward and centered on the Fe atom, as expected since the magnetism is mainly carried by the d electrons.

Nonlinear effects, i.e. $n_2(z)$, $P_2(z)$, etc, can be significant. In figure 2(b), the image plane position is seen to change significantly with field and clearly has nonlinear contributions. In the lower part of figure 2(a), the nonlinear charge contribution of $P_2(z)$, which determines the total SHG intensity, is seen to be almost completely outside the surface atomic layer; the fact that the spin contribution to $P_2$ does not vanish far into the bulk is indicative of the different response of the majority and minority spin channels to external electric fields.

Using the formulation of the external field in terms of external charges leads to a relationship between changes in work function with electric field and changes in the total energy. The change in total energy between the zero field and for a finite field corresponds to a change in electrons of $\Delta N$. The energy can be obtained by slowly building up the field:

$$\Delta E_{\text{tot}} = \int_0^{\Delta N} \mathrm{d}n \frac{\partial E_{\text{tot}}}{\partial n}. \tag{31}$$

But the derivative is simply the definition of the chemical potential $\mu$, so we have

$$\Delta E_{\text{tot}} = \int_0^{\Delta N} \mathrm{d}n \, \mu(\Delta N). \tag{32}$$

Because there is still a well-defined vacuum zero in this construction, the standard relationship between the chemical potential and work function, $\mu = -\phi$, holds.

Figure 3 demonstrates this analysis for Fe(001), where the total energy differences calculated directly and using equation (32) are compared; the agreement is excellent. This relationship between work function changes and total energy can be used, for example, to compare the difference in
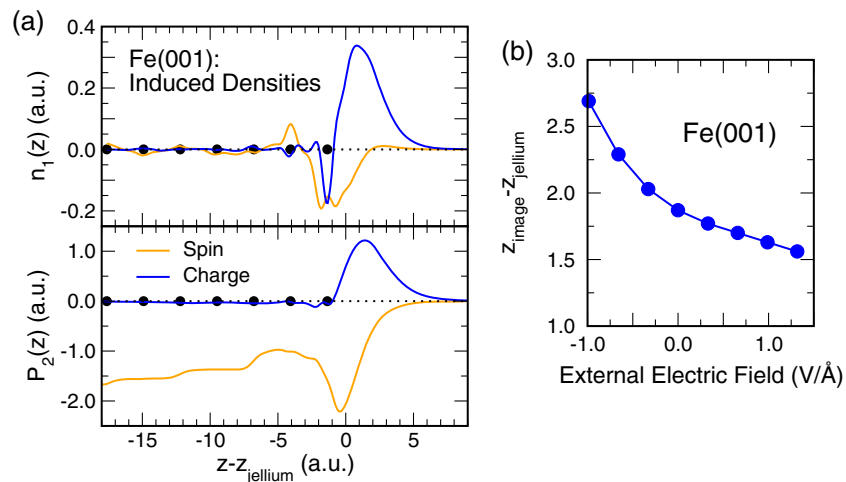


**Figure 2.** (a) Induced first-order charge and spin densities $n_1$ and second-order polarization $P_2$ for Fe(001). (b) Field dependence of the image plane position (in a.u.).
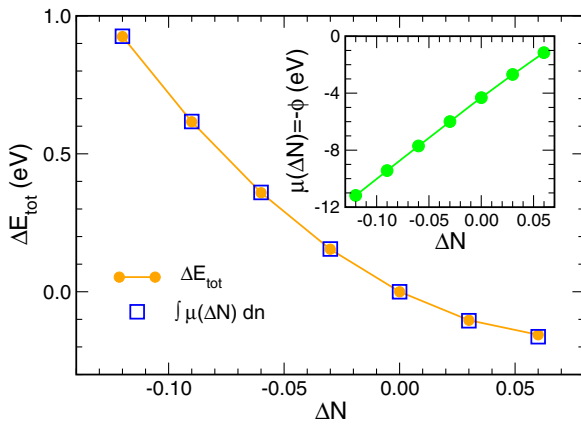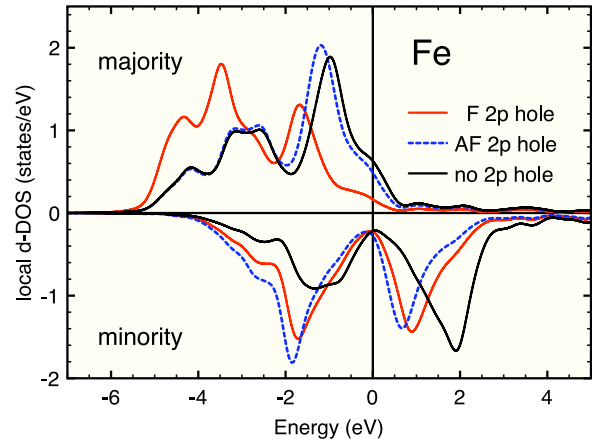
**Figure 3.** Total energy differences as a function of the external field expressed in terms of $\Delta N$ ($E = 4\pi\sigma = 4\pi \Delta N/A$) determined explicitly and as an integral of the work function/chemical potential. The calculated work function is shown in the inset.



**Figure 4.** Local d-like density of states of the central atom of a bulk Fe $3 \times 3$ supercell for the ground state (black solid line) and for a $2p_{3/2}$ electron excited just above $E_F$ ($= 0$ eV) with the remaining moment of the core electrons coupled either ferromagnetically (F; red solid line) or anti-ferromagnetically (AF; blue dotted line) to the valence electron moments.

anisotropy energies of magnetic systems in electric fields since—as a consequence of equation (32)—the work functions for different orientations of the spin magnetic moments in an electric field will differ.

## 5. Core holes

Treating core and valence states on an equal footing makes the FLAPW method particularly well suited to study core-level excitations from first principles. Particularly interesting are excitations where the influence of the generated core hole is immediately mirrored in the corresponding DOS, such as, for example, in the case of x-ray absorption or energy-loss near-edge spectra (ELNES). Usually the local excitation is modeled by the so-called $Z + 1$ approximation, where the higher nuclear charge of the excited atom is simulated by substituting it by the element to its right, i.e. with the $Z + 1$ atom. FLAPW, on the other hand, offers a direct route to the excitation if one includes a suitable constraint to deal with the excited core electron. Here we present a short study of the core hole effects in bulk bcc Fe when a $2p_{3/2}$ core electron is excited just above $E_F$. We model this event by using a $3 \times 3$ cubic supercell that guarantees that the core holes do not interact with each other and place the excited core electron of the central atom in the unoccupied valence states just above $E_F$. The total spin of the remaining core electrons may be coupled ferro- (F) or anti-ferromagnetically (AF) to the valence electrons which describes the excitation of a minority or majority spin core electron, respectively. In figure 4 the effect of the core hole on the d-like valence states is clearly visible. The largest effect is on the majority d-states if the remaining core electron spin is in the same direction, i.e. a minority core electron has been pushed above $E_F$. Obviously the majority valence states see a much less screened minority hole and are thus lowered in energy by the larger attraction of the nucleus. This reasoning is justified considering the small effect on the majority d-states when a majority core electron is excited, leaving behind a net core spin which is AF coupled

to the valence states. Here the screening is very efficient, producing a DOS almost indistinguishable from the case where no excitation is present. Turning now to the effect on the minority d-states we immediately see a similar large effect for the two possible core–valence spin couplings. The minority states are pulled down in energy and thus reduce the local moment on the excited Fe atom from a bulk value of 2.22 $\mu$B to 1.91 for F coupling and further to 1.41 for AF coupling. Clearly, in the latter case, the majority core electron pushed above $E_F$ has only a limited number of unoccupied majority d-states available, which leads to an enhanced occupation of the minority d-states in the screening process, reducing the spin moment even more. The effect of the different couplings on the spin–orbit splitting of the 2p states is negligible and the value calculated from total energy differences is 12.96 eV, which agrees very well with a measured value of 12.9 (13.2) eV [39]. The spin splitting due to the different couplings is much smaller than the spin–orbit splitting, namely 0.85 eV and from the total energies one learns, not quite unexpectedly, that the ferromagnetic coupling—the excitation of a minority core electron—is energetically favorable.

In figure 5 the effect of the core hole on the charge density is shown by taking the difference between the density before and after excitation with ferromagnetic coupling between core and valence electrons in a (110) plane through the excited atom. The difference density is a large black hole in the middle with a bright rim showing the screening charge. Due to the d-like nature of the screening electrons the screening charge is rather localized around the excited atom, and the contributions from the neighboring atoms are very small. A similar result is found for AF coupling and also for excitations from the $2p_{1/2}$ core level.

## 6. Defects and phase stability in Zr–Al alloys

The Zr–Al binary phase diagram [40, 41] is one of the most complicated, with 10 reported ordered phases ranging
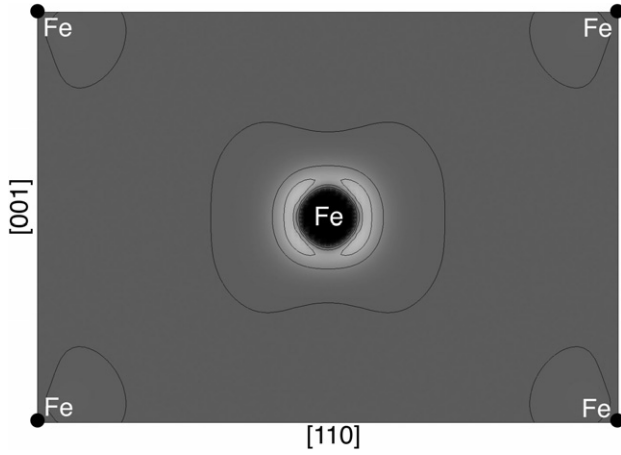
**Figure 5.** Difference density (excited–ground state) for the central region of a bulk bcc Fe $3 \times 3$ supercell. A $2p_{3/2}$ electron was excited just above $E_F$ with a ferromagnetic core moment coupling to the valence electrons. Black denotes regions of negative density and white of positive density. Zero is shown as gray.

from $ZrAl_3$ to $Zr_3Al$, all occurring in narrow composition ranges of the order of 1%. Of these phases, two are high-temperature phases and a number of the others decompose into other phases at high temperatures. The phase diagram is also complicated from a structural sense in that the various compounds are found [42] in hexagonal, orthorhombic, tetragonal and cubic structures. Because of the diversity of structures and competing phases, the Zr–Al system is a severe test of electronic structure theory. As shown previously [43], the overall properties of the low-temperature phase diagram are correctly reproduced and the existence of a large number of observed phases is attributed to the fact that the heats of formation for $Zr_xAl_{1-x}$ for $x = 0.25$–$0.75$ fall on a nearly straight line, suggesting that these phases should have narrow composition ranges.

Although the existence of the different phases can be understood from calculations of the ideal systems, to describe the concentration ranges and the temperature dependence of phases requires that one looks at the intrinsic defects (vacancies, antisites). In particular, the $Zr_3Al$ phase is stable only to $\sim 1260$ K. In this section, we will concentrate on the Zr-rich phases: $Zr_2Al$ (hP6), $Zr_3Al$ (fcc/$Cu_3Au$) and Zr (bcc, hcp), and determine the energetics of defect formation and phase stability. The approach we follow is to calculate the total energies of supercells of between 32 and 128 atoms to model isolated defects, and then use statistical mechanics to model the temperature dependence and off-stoichiometry. The calculations described here make use of *flair* and are consistent with the previous results [43] that used pseudopotentials that were 'tuned' to reproduce a number of all-electron results [44]; finding 'good' transferable pseudopotentials is non-trivial and involves a significant amount of art.

### 6.1. Statistical mechanics of independent defects

The general approach follows [45–47] for determining the statistical mechanics of an homogeneous binary $A_{1-x}B_x$ alloy

assuming non-interacting defects. We start from the grand potential $\Omega$ to allow for varying numbers $(N_A, N_B)$ of A and B atoms:

$$\Omega = U - TS - \mu_A N_A - \mu_B N_B, \tag{33}$$

where $\mu_i$, $i = A, B$ are the chemical potentials. If the ideal concentration of the compound is $x_0$, then for a system with $N$ sites, the total number of each type of atom will be

$$N_A = (1 - x_0)N - N_v^\alpha - N_B^\alpha + N_A^\beta \tag{34a}$$

$$N_B = x_0 N - N_v^\beta - N_A^\beta + N_B^\alpha, \tag{34b}$$

where $\alpha$ ($\beta$) denotes the 'A' ('B') nominal sublattice, $N_v^\alpha$ corresponds to the number of A vacancies and $N_B^\alpha$ to a B (antisite) atom on the $\alpha$ sublattice. The internal energy $U$,

$$U = N\epsilon_0 + N_v^\alpha \epsilon_v^\alpha + N_v^\beta \epsilon_v^\beta + N_B^\alpha \epsilon_B^\alpha + N_A^\beta \epsilon_A^\beta, \tag{35}$$

is given in terms of the bulk energy $\epsilon_0$ and the defect energies $\epsilon_i$ obtained from the differences in total energies between the (fully relaxed) supercell with the defect and the ideal systems (plus, possibly the pure A and B reference energies). To complete the specification of the grand potential, we need the chemical potentials and the entropy. The entropy has several contributions: vibrational, electronic and configurational. All of these (as we will see later) are important, but in the independent defect model, we limit ourselves to configurational entropy:

$$\frac{S}{k_B} = \sum_\alpha \ln \frac{(x_\alpha N)!}{N_v^\alpha! N_B^\alpha! (x_\alpha N - N_v^\alpha - N_B^\alpha)!}. \tag{36}$$

(Electronic entropy contributions can be calculated directly in the electronic structure calculations.)

Minimizing $\Omega$ with respect to $N_i^\alpha$ yields expressions for the concentration of defects:

$$c_v^\alpha = (1 - x_0) \frac{e^{(\epsilon_v^\alpha + \mu_A)/k_B T}}{1 + e^{(\epsilon_v^\alpha + \mu_A)/k_B T} + e^{(\epsilon_B^\alpha + \mu_A - \mu_B)/k_B T}} \tag{37}$$

$$c_B^\alpha = (1 - x_0) \frac{e^{(\epsilon_B^\alpha + \mu_A - \mu_B)/k_B T}}{1 + e^{(\epsilon_v^\alpha + \mu_A)/k_B T} + e^{(\epsilon_B^\alpha + \mu_A - \mu_B)/k_B T}}. \tag{38}$$

Because the number of atoms is free to vary, the overall composition $x$ of the alloy will be given by

$$\frac{1 - x}{x} = \frac{(1 - x_0) - c_v^\alpha - c_B^\alpha + c_A^\beta}{x_0 - c_v^\beta - c_A^\beta + c_B^\alpha}. \tag{39}$$

To complete the specification of the problem, we impose the Gibbs condition (at $P = 0$) relating the chemical potentials:

$$\mu_i = \left(\frac{\partial G}{\partial N_i}\right)_{P,T} \Rightarrow G = \sum_i \mu_i N_i = U - TS. \tag{40}$$

Given the various defect energies $\epsilon_i$, then for a given alloy concentration $x$ and temperature $T$, we need to (numerically) solve for the chemical potentials $\mu_i$.

The calculated defect energies $\epsilon_i$ are *not* the same as the thermodynamic defect formation energies, $\Delta H_f^d$, which are defined for a *constant number* of atoms:

$$\Delta H_f^d = \left(\frac{\partial G}{\partial N_d}\right)_{P,T,n_i}. \tag{41}$$

11
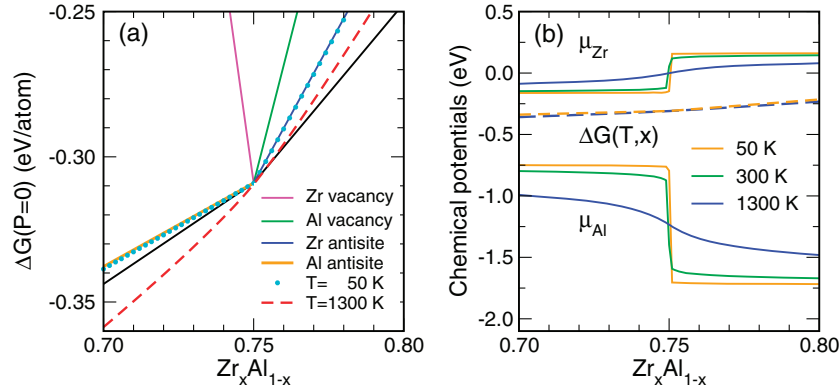
**Figure 6.** (a) The heat of formation (per atom) around $Zr_3Al$. Lowest solid (black) lines correspond to the tie lines connecting $Zr_3Al$ to $Zr_2Al$ and pure Zr. The solid lines show the effect on the heat of formation of different defects as a function of concentration. The free energy at $T = 50$ K (cyan dots) and at 1300 K (red dashed line) are also given. (b) The chemical potentials for Al and Zr as a function of concentration at $T = 50$, 300 and 1300 K. The corresponding Gibbs free energies (dashed lines) are also given.

**Table 1.** Low-temperature defect formation energies (eV) for $Zr_3Al$.

|         | Al vacancy | Zr vacancy | Al antisite | Zr antisite |
|---------|------------|------------|-------------|-------------|
| Al-rich | 2.61       | 2.02       | 0           | 1.32        |
| Zr-rich | 1.63       | 2.35       | 1.32        | 0           |

From the definitions, it is clear that the chemical potentials enter the defect formation energies, e.g.

$$\Delta H_v^i = \epsilon_v^i + \mu_i \tag{42}$$

$$\Delta H_\alpha^B = \epsilon_B^\alpha + \mu_A - \mu_B. \tag{43}$$

Stoichiometric defects may be pairs, triplets, etc, and will exist at finite temperatures.

### 6.2. Energetics of Zr-rich Zr–Al alloys

Figure 6(a) gives the calculated heats of formations from the supercell calculations for the various intrinsic defects in $Zr_3Al$. On both the Zr-and Al-rich sides, antisites are more stable than vacancies, and thus one should expect that changes in composition will be accommodated through antisites. Note that the heat for Al antisites is *more* bound than the ideal $x = 3/4$ system, i.e. the system gains energy by increasing the Al concentration. Although it might be tempting to deduce that there will be a broad concentration range on the Al-rich side, this is not the case since the tie line connecting $Zr_2Al$ is even more bound. As a general rule, to describe the thermodynamics of a given phase, it is essential to also consider competing phases.

The calculated Al and Zr chemical potentials as a function of concentration are given in figure 6(b). The chemical potentials are seen to depend on both $x$ and $T$, and have discontinuities (for $T = 0$) at $x_0$. Since the chemical potentials $\mu_i$ are measures of each component's relative contribution to the alloy heat, Al, as the minority component, is relatively more important to the binding. Conversely, for Zr-rich alloys, $\mu_{Zr} > 0$, indicating that increasing the concentration of Zr in this part of the compositional range decreases the overall

**Table 2.** Low-temperature defect formation energies (eV) for $Zr_2Al$ and hcp/bcc Zr.

|            | Al-rich |          | Zr-rich |          |
|------------|---------|----------|---------|----------|
| $Zr_2Al$ site | Vacancy | Antisite | Vacancy | Antisite |
| Al 2c      | 2.45    | 1.38     | 1.53    | 0        |
| Zr 2a      | 1.58    | 0        | 2.04    | 1.38     |
| Zr 2d      | 2.36    | 1.07     | 2.82    | 2.46     |
|            | Zr vacancy | Al antisite |       |          |
| hcp Zr     | 2.02    | 0        |         |          |
| bcc Zr     | 0.83    | 0        |         |          |

binding. These results demonstrate clearly that the often invoked heuristic of dividing the total heat of formation evenly among the constituents is too simplistic. Moreover, since the chemical potentials can vary by several eV as a function of concentration, the chemical potentials vary during the growth process for approaches such as molecular beam epitaxy (MBE), even though the external conditions remain constant. This observation has important implications for the modeling of growth and relating experimental conditions to quantities that can be (easily) calculated.

The low-temperature defects for $Zr_3Al$ are given in table 1. The compositional/constituent defects (those with zero formation energy at $T = 0$) are antisites on both sides of $x_0 = 3/4$. Thus, at low temperatures, changes in stoichiometry are accommodated by antisites, with few vacancies. As the temperature increases, the concentration of vacancies, shown in figure 7(b), also increases. In addition, the defect formation energies of figure 7(a) are likewise temperature-dependent, with the result that the non-constituent defects become more likely, driven by the entropic contributions.

As seen in figure 7, at stoichiometry ($x_0 = 3/4$) defects also occur, but they must occur in groups in order to maintain the correct composition. The simplest stoichiometric complexes at $x_0$ and their energies (per defect) are: (i) double antisite (1 Zr antisite + 1 Al antisite): 0.66 eV; (ii) 3 Zr + 1 Al vacancies: 2.17 eV; (iii) Zr antisite complex (1 Zr antisite + 4 Zr vacancies): 1.88 eV and (iv) Al antisite complex
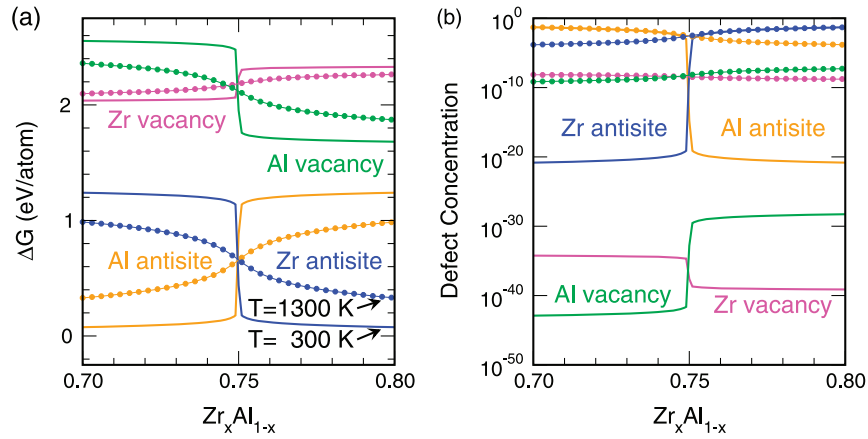
**Figure 7.** Calculated (a) defect formation energies ($\Delta G$) and (b) defect concentrations for the intrinsic (vacancies, antisites) defects for $Zr_3Al$ at $T = 300$ and 1300 K.

(3 Al antisites + 4 Al vacancies): 1.49 eV. Not surprisingly, the double antisite is the most likely stoichiometric defect. Moreover, note that these formation energies are the same regardless of whether the Al- or Zr-rich individual defect formation energies of table 1 are used, thus providing a necessary consistency check on the formation energies.

From the calculated chemical potentials, defect concentrations, etc, the free energy as a function of concentration around $x_0$ can be determined and are shown for $T = 50$ and 1300 K in figure 6(a). For low temperatures, the free energy (adjusted to agree with the $T = 0$ energy at $x_0$) follows the antisite curves. For high temperature (1300 K) and $x > x_0$, the free energy lies above the $T = 0$ tie line, indicating that Zr-rich alloys are not expected in this structure. For the Al-rich part of the phase diagram, the free energy lies below the $T = 0$ tie line to $Zr_2Al$, allowing for the possibility of Al-rich alloys. However, to be consistent, it is necessary to consider the free energies (and hence the intrinsic defects) of the competing phases, i.e. $Zr_2Al$ and Zr.

The hP6 $Zr_2Al$ structure has two inequivalent Zr sublattices. The statistical mechanics are treated using an obvious generalization of the formalism described above; the resulting defect formation energies are given in table 2. For Al-rich alloys ($x < x_0$), there is a strong site preference (~1 eV) for Al antisites on the 2a sublattice because that maximizes the number of Zr neighbors for the additional Al atoms. On the Zr-rich side ($x > x_0$, towards $Zr_3Al$), the preference is for Zr antisites on the single Al sublattice.

For pure Zr, the observed low-temperature phase is hcp, and then transforms at higher temperatures (830 K) to bcc, with both phases showing significant ranges of Al solubility. Since to change the concentration $x$ requires the addition of Al, the constituent defects for both phases are Al antisites, and the Al chemical potentials are $-0.88$ and $-0.64$ eV for the hcp and bcc phases, respectively, favoring the alloying of Al into pure Zr. The cost for generating Zr vacancies is significantly lower for bcc Zr compared to hcp. This cost, plus the accompanying large (~10%) relaxations for the bcc vacancy, are related to the bcc lattice instabilities.

Combining the results from the calculations for $Zr_2Al$, $Zr_3Al$ and Zr, one can determine composition ranges. The

experimental maximum of the Al solubility limit in hcp Zr of ~11% occurs at 1200 K. The calculated Al solubility limits are around zero at room temperature, 0.1% at 600 K, 1.2% at 1000 K and 3.5% at 1300 K. While the trend of increasing solubility is correct, the overall magnitude is too small. (There is no calculated width for Zr-rich $Zr_3Al$.)

In addition to the solubility limits issue, the calculated energy differences between hcp and bcc Zr as a function of temperature continue to favor hcp Zr far above the observed transition. To resolve these discrepancies requires the inclusion of vibrational entropy contributions.

To describe the disappearance of the $Zr_3Al$ phase at ~1260 K—$Zr_3Al \leftrightarrow Zr_2Al + \beta Zr$ (with 12% Al)—we allow for relative shifts of $\Delta G$ for different structures to account for electronic and vibrational entropy contributions. The electronic entropy contributions to the relative phase stability of phase $P$ relative to fcc $Zr_3Al$, $\Delta S_e = S_e[P] - S_e[Zr_3Al]$, are easily obtained from the standard electronic structure calculations: $0.04k_B$ for $Zr_2Al$, $0.32k_B$ for bcc Zr and $0.13k_B$ for hcp Zr. The requirements that, at $T = 1300$ K (i) bcc Zr be more stable than hcp, (ii) $Zr_3Al$ is unstable to $Zr_2Al$ and Zr, and (iii) the Al solubility is ~10%, yields estimates of the vibrational entropy differences, $\Delta S_V$, relative to $Zr_3Al$ of $0.14k_B$ for $Zr_2Al$, $0.48k_B$ for bcc Zr and $0.04k_B$ for hcp Zr, and with these values, the Zr–Al phase diagram at the Zr-rich end (cf. figure 8) is correctly reproduced. The value of $\Delta S_V$ for bcc Zr is comparable to the Friedel estimate of $0.6k_B$ between close-packed (fcc/hcp) and bcc structures, as well as the experimental estimate of $0.5–0.6k_B$ for the bcc–hcp Zr transition. Moreover, since $Zr_2Al$ is not close-packed (especially the 2a site), this value of $\Delta S_V$ is also plausible. In principle, the vibrational contributions to the free energies can also be calculated directly, including for the defect structures, but that is beyond the scope of the present paper.

Based on these results, a number of conclusions can be drawn. Antisites are the compositional defects for Zr-rich Zr–Al alloys, with few vacancies at normal temperatures; and for $Zr_2Al$, there is a pronounced site preference (2a) for Al antisites. Proper treatment of intrinsic defects are necessary to describe phase stability, with the composition
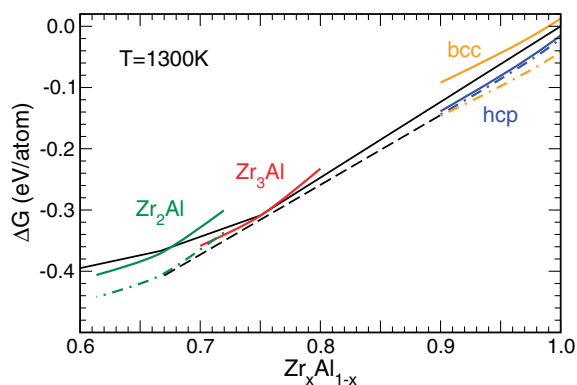
**Figure 8.** Free energies (relative to Zr$_3$Al), including configurational and electronic entropies (——), and free energies with the addition of the vibrational entropies (— · —) at $T = 1300$ K for the Zr$_2$Al, Zr$_3$Al, and bcc and hcp Zr phases. The $T = 0$ (continuous black solid line) and $T = 1300$ K tie lines are also given.

widths depending on the properties of each individual phase, plus the relative energies. The values of $\Delta S_V$ extracted by demanding that Zr$_3$Al becomes unstable are reasonable.

## 7. Summary

The modifications and extensions described here (along with others) make the FLAPW method, as implemented in *flair* [12], easy to use and applicable to an ever wider variety of new and complex materials. We have illustrated the utility of the method by calculations of the induced densities in external fields, magnetic coupling between core holes and valence states, and the effect of intrinsic defects on the phase stability of Zr–Al alloys. With the on-going development and an active user base, the FLAPW approach will continue to play an important role in materials design.

## Acknowledgments

## References

[1] Kohn W and Sham L J 1965 *Phys. Rev.* **140** A1133
[2] Slater J C 1937 *Phys. Rev.* **51** 846
[3] Marcus P M 1967 *Int. J. Quantum Chem. Suppl.* **1** 567
[4] Andersen O 1975 *Phys. Rev.* **12** 2060
[5] Koelling D D and Arbman G O 1975 *J. Phys. F: Met. Phys.* **5** 2041
[6] Krakauer H, Posternak M and Freeman A J 1979 *Phys. Rev. B* **19** 1706
[7] Weinert M 1981 *J. Math. Phys.* **22** 2433
[8] Hamann D R 1979 *Phys. Rev. Lett.* **42** 662
[9] Wimmer E, Krakauer H, Weinert M and Freeman A J 1981 *Phys. Rev. B* **24** 864
[10] Weinert M, Wimmer E and Freeman A J 1982 *Phys. Rev. B* **26** 4571
[11] Yu R, Singh D J and Krakauer H 1991 *Phys. Rev. B* **43** 6411
[12] Weinert M, Schneider G, Podloucky R and Redinger J http://www.uwm.edu/~weinert/flair.html
[13] Blügel S and Bihlmayer G http://www.flapw.de
[14] Freeman A J *et al* http://flapw.com
[15] Blaha P, Schwarz K, Madsen G, Kvasnicka D and Luitz J http://www.wien2k.at
[16] Singh D J 1991 *Phys. Rev. B* **43** 6388
[17] Fernando G W, Davenport J W, Watson R E and Weinert M 1989 *Phys. Rev. B* **40** 2757
[18] Watson R E, Weinert M and Fernando G W 1991 *Phys. Rev. B* **43** 1446
[19] Abramowitz M and Stegun I A 1964 *Handbook of Mathematical Functions* (Washington, DC: National Bureau of Standards) 1972, 10th printing, with corrections
[20] Danos M and Maximin L C 1965 *J. Math. Phys.* **6** 766
[21] Blöchl P E 1994 *Phys. Rev. B* **50** 17953
[22] Kresse G and Joubert D 1999 *Phys. Rev. B* **59** 1758
[23] Cardona M and Pollak F H 1966 *J. Phys. Chem. Solids* **27** 423
    Rastl P 1975 *PhD Thesis* Univ. Vienna (in German)
[24] Lang N D 1969 *Solid State Commun.* **7** 1047
[25] Lang N D and Kohn W 1970 *Phys. Rev. B* **3** 1215
[26] Inglesfield J E 1987 *Surf. Sci.* **188** L701
[27] Aers G C and Inglesfield J E 1989 *Surf. Sci.* **217** 367
[28] Weber M G and Liebsch A 1987 *Phys. Rev. B* **35** 7411
    Weber M G and Liebsch A 1987 *Phys. Rev. B* **36** 6411
[29] Gies P and Gerhardts R R 1985 *Phys. Rev. B* **31** 6843
    Gies P and Gerhardts R R 1986 *Phys. Rev. B* **33** 982
[30] Weinert M 1991 *Bull. Am. Phys. Soc.* **36** 751
    Weinert M, unpublished
[31] Erschbaumer H, Podloucky R and Neckel A 1990 *Surf. Sci.* **237** 291
[32] Heinze S, Nie X, Blügel S and Weinert M 1999 *Chem. Phys. Lett.* **315** 167
[33] Schneider G and Weinert M 2000 http://flux.aps.org/meetings/YR00/MAR00/abs/S7500.html
[34] Erschbaumer H 1988 *PhD Thesis* Univ. Vienna (in German)
[35] Smith N V, Chen C T and Weinert M 1989 *Phys. Rev.* **40** 7565
[36] Bengtsson L 1999 *Phys. Rev. B* **59** 12301
[37] Neugebauer J and Scheffler M 1993 *Surf. Sci.* **287/288** 572
[38] Meyer B and Vanderbilt D 2001 *Phys. Rev. B* **63** 205426
[39] Fink J, Müller-Heinzerling Th, Scheerer B, Speier W, Hillebrecht F U, Fuggle J C, Zaanen J and Sawatzky G A 1985 *Phys. Rev. B* **32** 4899
[40] McPherson D J and Hansen M 1954 *Trans. Am. Soc. Met.* **46** 354
    Pöstchke M and Schubert K 1962 *Z. Metallkd.* **53** 549
    Murray J, Peruzzi A and Abriata J P 1992 *J. Phase Equilib.* **13** 277
    Peruzzi A 1992 *J. Nucl. Mater.* **186** 89
[41] Massalski T 1990 *Binary Alloy Phase Diagrams* 2nd edn (Metals Park, OH: American Society for Metals)
    Predel B 1991 *Landolt–Börnstein New Series* vol IV/5a (Berlin: Springer)
[42] Villars P and Calvert L D 1991 *Pearson's Handbook of Crystallographic Data for Intermetallic Phases* 2nd edn (Metals Park, OH: American Society for Metals)
[43] Alatalo M, Weinert M and Watson R E 1998 *Phys. Rev. B* **57** R2009
[44] Alatalo M, Weinert M and Watson R E 1999 *Phys. Rev. B* **60** 7680
[45] Mayer J, Elässer C and Fähnle M 1995 *Phys. Status Solidi* b **191** 283
[46] Meyer B and Fähnle M 1999 *Phys. Rev. B* **59** 6072
[47] Rasamny M, Weinert M, Fernando G W and Watson R E 2001 *Phys. Rev. B* **64** 144107